



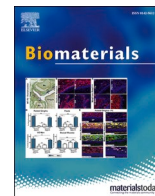
Vascularization of tissue engineered cartilage - Sequential in vivo MRI display functional blood circulation

Downloaded from: <https://research.chalmers.se>, 2025-12-05 03:11 UTC

Citation for the original published paper (version of record):

Apelgren, P., Amoroso, M., Säljö, K. et al (2021). Vascularization of tissue engineered cartilage - Sequential in vivo MRI display functional blood circulation. *Biomaterials*, 276. <http://dx.doi.org/10.1016/j.biomaterials.2021.121002>

N.B. When citing this work, cite the original published paper.



Vascularization of tissue engineered cartilage - Sequential in vivo MRI display functional blood circulation

Peter Apelgren^{a,b,*}, Matteo Amoroso^{a,b}, Karin Säljö^{a,b}, Mikael Montelius^c, Anders Lindahl^d, Linnea Stridh Orrhult^e, Paul Gatenholm^e, Lars Kölby^{a,b}

^a Department of Plastic Surgery, Institute of Clinical Sciences, Sahlgrenska Academy, University of Gothenburg, Gothenburg, Sweden

^b Region Västra Götaland, Sahlgrenska University Hospital, Department of Plastic Surgery, Gothenburg, Sweden

^c Department of Radiation Physics, Institute of Clinical Sciences, Sahlgrenska Academy, University of Gothenburg, Gothenburg, Sweden

^d Department of Clinical Chemistry and Transfusion Medicine, Institute of Biomedicine, Sahlgrenska Academy, Gothenburg, Sweden

^e 3D Bioprinting Centre, Department of Chemistry and Chemical Engineering, Chalmers University of Technology, Gothenburg, Sweden

ARTICLE INFO

Keywords:

3D bioprinting
MRI
In vivo
Chondrocytes
Cartilage
DWI
Vascularization
Angiogenesis

ABSTRACT

Establishing functional circulation in bioengineered tissue after implantation is vital for the delivery of oxygen and nutrients to the cells. Native cartilage is avascular and thrives on diffusion, which in turn depends on proximity to circulation. Here, we investigate whether a gridded three-dimensional (3D) bioprinted construct would allow ingrowth of blood vessels and thus prove a functional concept for vascularization of bioengineered tissue. Twenty $10 \times 10 \times 3$ -mm 3Dbioprinted nanocellulose constructs containing human nasal chondrocytes or cell-free controls were subcutaneously implanted in 20 nude mice. Over the next 3 months, the mice were sequentially imaged with a 7 T small-animal MRI system, and the diffusion and perfusion parameters were analyzed. The chondrocytes survived and proliferated, and the shape of the constructs was well preserved. The diffusion coefficient was high and well preserved over time. The perfusion and diffusion patterns shown by MRI suggested that blood vessels develop over time in the 3D bioprinted constructs; the vessels were confirmed by histology and immunohistochemistry. We conclude that 3D bioprinted tissue with a gridded structure allows ingrowth of blood vessels and has the potential to be vascularized from the host. This is an essential step to take bioengineered tissue from the bench to clinical practice.

One sentence summary

In this study, we used functional MRI methods to visualize the development of vascularization in 3D bioprinted constructs.

1. Introduction

Reconstructing damaged or absent cartilaginous facial structures, such as the nose and auricle, is a challenge for the reconstructive surgeon, as cartilage has limited ability to heal and regenerate [1]. The gold standard is transplantation of autologous cartilage grafts from another location (e.g., ribs) after manual sculpturing [2,3]. These procedures are tedious and multistaged, and often cause pain, infection, and disfigurement [4,5]. Three-dimensional (3D) bioprinting technology offers methods to circumvent these problems by using autologous chondrocytes mixed with a biomaterial scaffold that can be printed in the

desired shape, facilitating cell proliferation and tissue restoration and potentially simplifying the reconstruction.

Reconstruction of lost tissue often requires skin, cartilage, or bone substitutes that are considerably larger than can be supported by passive diffusion. Chondrocytes are dependent on the diffusion of oxygen and nutrients from blood vessels within 100–200 μm [6–8]. Therefore, construct size is a major limiting factor for sufficient nutrient supply, and vascular network formation is crucial [9,10]. Various approaches have been explored to overcome these limitations, including altering the geometry and porosity of the scaffold [11–18], using biomimetic vessels, and incorporating endothelial and smooth muscle cells, as well as growth factors needed for the vascular build-up [8,19–24]. To create larger viable implants, vessels generated de novo from endothelial cells (vasculogenesis) [25] must connect to the systemic circulation [26–32]. We hypothesize that angiogenesis—blood vessel formation assisted by germination from existing vessels—can be stimulated by using gridded

* Corresponding author. Department of Plastic Surgery, Institute of Clinical Sciences, Sahlgrenska Academy, University of Gothenburg, Gothenburg, Sweden.

E-mail address: peter.apelgren@vgregion.se (P. Apelgren).

<https://doi.org/10.1016/j.biomaterials.2021.121002>

Received 30 April 2021; Received in revised form 21 June 2021; Accepted 28 June 2021

Available online 7 July 2021

0142-9612/© 2021 The Authors. Published by Elsevier Ltd. This is an open access article under the CC BY license (<http://creativecommons.org/licenses/by/4.0/>).

constructs [33]. Many studies have reported signs of internal blood circulation in 3D bioprinted constructs [31], as judged from their survival over time and the absence of necrotic areas, but the vascularization of such constructs has not been visualized longitudinally in vivo.

MRI-based techniques are widely used to assess the perfusion and diffusion properties of native tissues [34–38]. Dynamic contrast-enhanced MRI (DCE-MRI) can assess tissue perfusion non-invasively. After intravenous injection of contrast agent, the MR signal increases in proportion to the concentration of the agent reaching a voxel (volume pixel). Functional characteristics of the vasculature can be derived by studying the voxel signal before, during, and after contrast administration. Mathematical tissue models can be used to extract quantitative parameters of, for example, vascular features such as permeability surface area product and the transfer rates between the extra- and intracellular space. Such models have been extensively used to predict and assess the therapeutic response of solid tumors [39]. However, this approach requires knowledge of the magnetic relaxation properties of the studied tissue and the arterial input function.

A more straightforward approach is to study semiquantitative features of the signal behavior. The arrival time (AT)—the time for MR signal amplitude to increase above baseline levels—can provide indirect information on oxygen and nutrient transport from the vasculature. A short AT indicates an adequately functional vasculature. Similarly, the initial slope (IS) of the increasing MR signal after contrast has reached the tissue reflects the rate at which contrast enters the interstitial space. A high IS indicates higher tissue oxygenation, as shown in an animal tumor model [40].

Nutrient and oxygen transport from the vasculature to cells by diffusion is slowed by cellular membranes and macromolecules in the extracellular space and by the viscosity of the extracellular fluid. Diffusion-weighted MRI (DWI) can be used to measure the restriction on molecular diffusion by sensitizing the MR signal to the motion of water molecules and by using so-called diffusion gradients and varying their effects in repeated DWI acquisitions. The diffusion coefficient can then be determined for each voxel by fitting a monoexponential model to the DWI signal decay with increased diffusion weighting. MR techniques are noninvasive and suitable for the longitudinal assessment of tissues and organs. Both DCE and DWI MRI are clinically translatable techniques and are therefore suitable for this project.

The three main bioprinting techniques, all of which build structures layer by layer, are extrusion [41–43], laser-assisted [44–46], and inkjet printers [21,47,48]. The extrusion bioprinting technique used in this study has the advantage of being able to use high-viscosity bioinks with high cell densities. Cellular structures and cell viability can be preserved by keeping the extrusion pressure and the shear stress as low as possible in the nozzle [49,50].

The characteristics and geometry of the bioink allow nutrient transport and cell migration, which is also important. Hydrogel, mainly consisting of water, promotes passive transport of nutrients and oxygen because of its viscosity and permeability properties [51]. After printing with nanocellulose bioink containing alginate, gelation is initiated with calcium chloride crosslinking. Nanocellulose-alginate bioink has the desired characteristics for printing complex structures, such as auricles [49], is compatible with human cells [52], and has been used to create cartilage-like constructs [53]. In previous in vivo studies, we showed that chondrocytes survive and proliferate in structure bioprinted from nanocellulose-alginate bioink, eventually forming cartilage-like tissue [54]. The constructs supported full-thickness skin grafts, making it possible to reconstruct composite structures [55]. Several hydrogels have been studied to recreate cartilaginous structures, such as collagen [30], alginate [56], hyaluronic acid [57], and synthetic hydrogels such as polyethylene glycol [58]. In this study, we used nanocellulose produced by tunicates. This ultra-pure hydrogel (>99% nanocellulose) has extraordinary rheological properties and excellent printability [59–61]. Nanocellulose has been approved for human applications by the FDA.

A critical step to take bioengineered tissue into clinical practice is the

vascularization of the constructed tissues. Previously, we showed that 3D bioprinted cartilage constructs in vivo become encapsulated by a thin layer of host connective tissue containing blood vessels [54,55]. The diffusion range is thus dependent on the diameter of the construct. In this study, we implanted 3D bioprinted constructs with a gridded structure into nude mice and used noninvasive MRI techniques to investigate oxygen and nutrient transport and vascularization of the constructs.

2. Results

2.1. Mice

Twenty 8-week-old female BALB/c nude mice were randomly assigned to receive implants that contained human nasoseptal chondrocytes or were cell-free. Two mice in the cell-free implant group developed ulcerations at the site of the tail catheter and were euthanized prematurely. However, the implants were retrieved for histologic analysis, and the MRI data from both mice were used in the overall analyses. The study protocol is provided in Table S1.

2.2. Magnetic resonance imaging

Fifteen mice were imaged at day 0 (9 cell-containing and 6 cell-free) and the images were briefly analyzed for technical quality (e.g., susceptibility artifacts, such as surgery-related subcutaneous air bubbles). Six mice in the cell-free group underwent 2 or 3 sequential MRI experiments (days 0, 30, and/or 90), and 6 carrying chondrocyte-containing constructs were imaged at all four time points (days 0, 7, 30, and 90). The MRI data of the mice in the cell-containing group are summarized in Fig. 1 and Fig. S3. Representative MR images from one mouse in the cell-free group are shown in Fig. S4.

Supplementary video related to this article can be found at <https://doi.org/10.1016/j.biomaterials.2021.121002>

2.3. Perfusion

The parametric maps of AT and initial slope IS on day 0 revealed longer AT and lower IS in all the printed constructs than in surrounding tissues. However, on day 30, five of the six cell-containing constructs had hot spots of shorter AT and higher IS at grid hole locations (Fig. 1 and Movie S1B). AT and IS maps of the sixth construct were more homogenous and had no hot spots (Fig. S3). The initial variation in MR signal intensity in the hot spots after contrast administration was similar to that of the aorta, suggesting a close connection to the systemic circulation (Fig. 2). However, during the wash-out phase, the contrast agent remained in the implants longer than in the surrounding tissue. On day 30, the median signal intensity in the hot spots increased approximately 130% after contrast injection, whereas the median volume signal intensity only increased 110% (data not shown). In the last session (day 90), the overall perfusion patterns were more homogenous and only one of the constructs had vaguely preserved hot spots (Fig. S3D). The cell-free constructs had no hot spots at any time (Fig. S4, S8 and S9 Movie S2).

2.4. Diffusion

The median diffusion coefficient was similar in the cell-containing constructs and the cell-free controls (2.56, interquartile range 2.16–2.97 vs. 2.58, interquartile range 2.24–2.89 $\mu\text{m}^2/\text{ms}$, respectively) (Fig. 3). The diffusion coefficient remained stable over time (Fig. 4).

2.5. Morphologic analysis

Macroscopic analyses of the explanted constructs revealed blood vessels sprouting on the surface of the constructs in both groups (Fig. 5

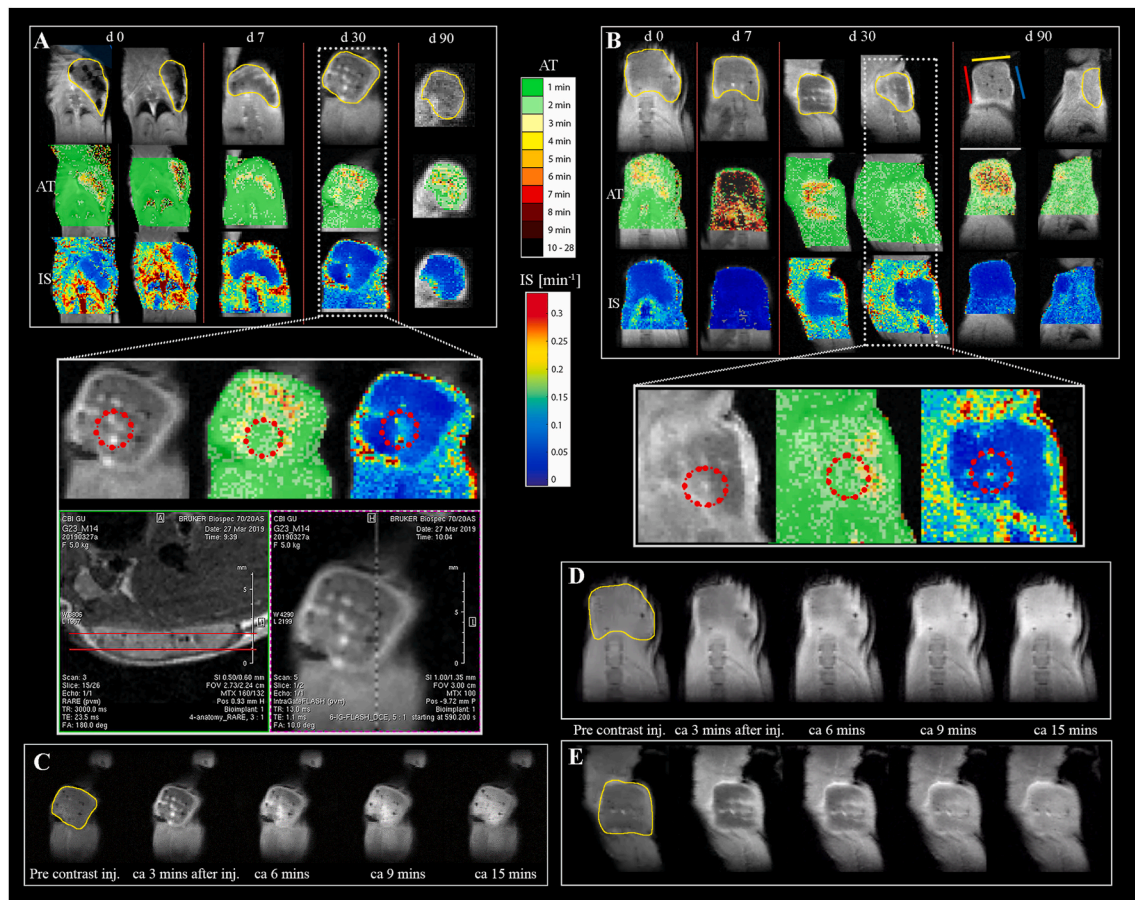


Fig. 1. DCE MRI signal intensity enhancement and parametric maps. Two chondrocyte-containing constructs and the MRI measurements for days 0, 7, 30, and day 90. The most significant and visually clear images from either sagittal or coronal planes are presented (**A** and **B**) and the constructs are outlined in yellow. Color-coded parametric maps of AT and IS reveal several local hot spots (short AT and/or high IS) on day 30 (circled in red). (**C–E**) The original DCE images used to derive the parametric maps are shown for selected time points after contrast injection. The contrast dynamics, with a build-up of local hot spots, are shown for day 0 (**D**) and day 30 (**E**) (Movies S1 and S2). Three minutes after injection of the contrast agent at day 30, the hot spots appear. 9 min after injection, the contrast agent gradually dissipates and the hot spot intensity declines. (For interpretation of the references to color in this figure legend, the reader is referred to the Web version of this article.)

and Fig. S6). The cell-containing constructs were well preserved, whereas some of the cell-free controls lost their shape and grid structure (Fig. S2) and were more fragile and more difficult to handle surgically. Microscopic analysis of cell-containing constructs stained with hematoxylin-eosin revealed a predominantly homogenous morphology, preserved grid holes, and vascular structures containing erythrocytes (Fig. 5). In some areas, we observed infiltration of connective tissue in the biomaterial beyond the grid holes. Alcian Blue van Gieson (ABvG) staining revealed chondrocyte clusters surrounded by glycosaminoglycans (GAG) (Fig. 5B), and Safranin-O staining confirmed the production of proteoglycans in the extracellular matrix (Fig. 5C). No GAG- or proteoglycan-producing cells were found in cell-free constructs (Fig. S6). None of the constructs had necrotic areas or histological signs of ossification or tumors. The hot spots displayed by perfusion MRI corresponded well to the vascularized grid holes (Fig. 5D).

2.6. Immunohistochemistry

Analysis for the endothelial cell marker CD31 showed a high density of vascular structures, mainly in the grid holes and in the capsule of the constructs (Fig. 5E). The immunohistochemical analysis for type 2 collagen corresponded well to the GAG-positive areas (Fig. 5F and G and Fig. S7). Additionally, to evaluate possible endochondral ossification, we conducted a supplemental analysis using silver nitrate staining for calcification and immunohistochemical analyses for type X collagen

(Fig. S10–12). No signs of hypertrophic transformation or endochondral ossification were detected.

Bars, 1000 μm (B, C), 500 μm (E, F, G), 100 μm (1, 2, 3) and 50 μm in the E magnification. Immunohistochemical analysis of a cell-free construct is shown in Fig. S6. Isotype comparison and raw images of F in Fig. S7. High-resolution magnifications of F in Fig. S13. The images A–G and 1, 2, 3 were cropped and linearly adjusted for contrast and exposure time.

3. Discussion

In this study, DWI and DCE-MRI were used to analyze the diffusion and perfusion properties of gridded 3D bioprinted constructs in nude mice *in vivo* over 90 days. Our findings show that functional blood vessels formed inside the 3D bioprinted tissues, providing the necessary vascular proximity needed for oxygen and nutrient transport to the chondrocytes. Thus, the constructs have the potential to be vascularized from the host—an essential step toward the clinical use of bioengineered tissue to reconstruct cartilaginous facial structures.

The gridded geometrical structure of the bioinks may be a key feature facilitating the growth of blood vessels and, in combination with a permeable biomaterial, such as tunicate nanocellulose/alginate, may create an advantageous micromilieu for chondrogenesis. No necrotic areas were detected by histology or *in vivo* DWI, suggesting sufficient delivery of oxygen and nutrients. The DWI analysis proved that the

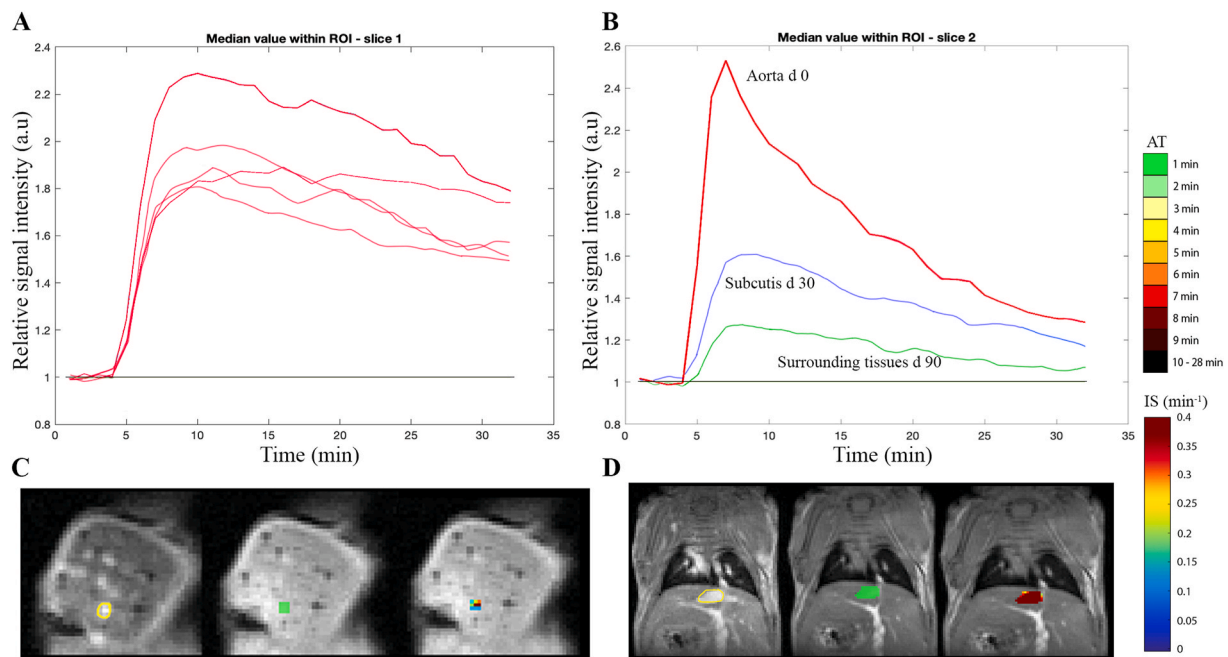


Fig. 2. Hot spot perfusion. (A and B) Comparison of signal intensity curves in hot spots (A) to that of the aorta (B) suggests that vessels in hot spots are closely interconnected with the systemic circulation. During the wash-out phase, however, the contrast agent remained longer in the constructs than in the surrounding tissue. (C and D) DCE sequence of a representative cell-containing construct at day 30 (C) and the aorta (D). ROIs are delineated in yellow and encompass one hot spot (C) and central parts of the aorta (D). AT (C and D middle), and IS (C and D right). Color bars indicate the AT in minutes after injection and the increase in IS signal intensity per unit of time. (For interpretation of the references to color in this figure legend, the reader is referred to the Web version of this article.)

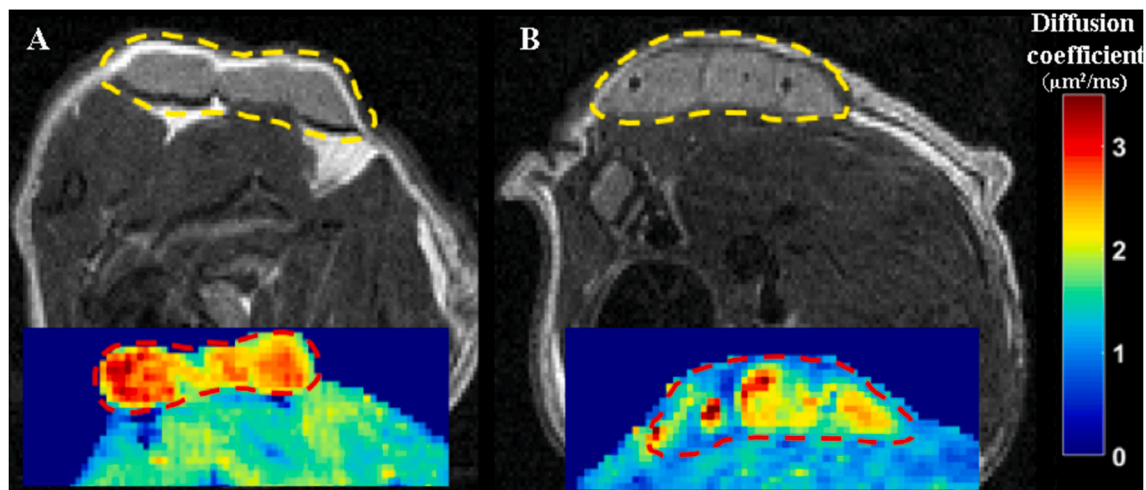


Fig. 3. Diffusion. (A and B) T2-weighted, axial images of two representative mice, bearing cell-free (A) and chondrocyte-containing (B) implants (outlined in yellow) on day 30. Inserted parametric maps show the corresponding color-coded diffusion coefficient. The median and interquartile range of the diffusion coefficient were determined for each implant by manually delineating visible implant on all images, avoiding air/fluid pockets and artifacts. The median diffusion coefficient and interquartile range were 2.73 (2.37 – 3.02) $\mu\text{m}^2/\text{ms}$ in the cell-free construct and 2.34 (2.07 – 2.65) $\mu\text{m}^2/\text{ms}$ in the chondrocyte-containing construct. The slight misalignment between the diffusion maps and the anatomical images was caused by susceptibility differences between air and tissue, affecting the DWI measurements. The color bar indicates the diffusion coefficient in $\mu\text{m}^2/\text{ms}$. (For interpretation of the references to color in this figure legend, the reader is referred to the Web version of this article.)

diffusion properties of the TNC biomaterial prevailed over time, suggesting that TNC is highly suitable for tissue engineering. Furthermore, the shape, dimensions, and solidity of the constructs were better preserved in those containing cells; the cell-free constructs were more fragile and tore more easily.

DCE and DWI-MRI are promising tools to assess vascularization in 3D bioprinted nanocellulose-based constructs and might be valuable for postoperative monitoring of 3D bioprinted implants. The quality and resolution of the MR images were, with few exceptions, excellent, and

could distinguish small variances in perfusion and diffusion between different parts of the constructs. Zhou et al. reviewed ultrasound applications in 3D bioprinting, including visual assessment of vascularization [62]. Although ultrasound offers cheaper equipment and may be more readily available and easier to operate, it lacks the soft tissue contrast and resolution offered by MRI, which are major disadvantages. Furthermore, computed tomography (CT), including angiography and micro-CT, has been used because of its high spatial resolution but also lacks the required soft tissue contrast. Additionally, radiation from

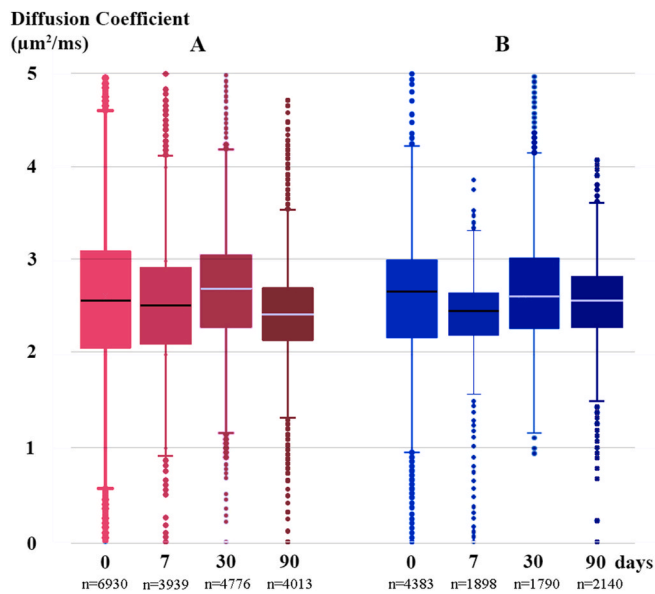


Fig. 4. Diffusion coefficient. (A and B) The median diffusion coefficient (D) was relatively stable over the study period without obvious trends in the cell-containing (A) or the cell-free (B) constructs. The median pooled diffusion coefficient (all time points and voxels) was 2.56 (interquartile range 2.16–2.97) $\mu\text{m}^2/\text{ms}$ for the cell-containing constructs and 2.58 (2.24–2.89) $\mu\text{m}^2/\text{ms}$ for the cell-free constructs. The diffusion data are from 29,877 samples (n = number of voxels). Lines inside the boxes indicate the median; box edges indicate interquartile range. Whiskers extend to maximum and minimum values; outliers are presented as dots outside the whiskers.

repeated examinations may affect the radiosensitive cells involved in vascularization [63].

Initially, AT was long, and IS was low in the printed constructs, indicating lower perfusion than in surrounding tissues. Over time, however, signal intensity hot spots appeared in five of the six cell-containing constructs, corresponding perfectly to the grid holes. The AT in the hot spots was comparable to that in the aorta; thus, vessels in the bioprinted construct were integrated with the systemic circulation of the host. The cell-free constructs appeared to be generally more homogeneous on the parametric maps of AT and IS at all time points, and no hot spots developed. In the cell-containing constructs at day 90, the hot spots were indistinguishable, but the overall perfusion had improved and in major parts of the constructs was comparable to that in surrounding tissues.

This observation suggests that by day 90, a neovascular network had been established in which a few single supplying vessels in the grid holes were less dominant, and the blood flow was more evenly distributed over a larger number of smaller vessels that could not be detected as hot spots. This interpretation is supported by morphological and immunohistochemical evidence that blood vessels were distributed throughout the grid holes. The vessels contained erythrocytes, confirming the connection to the systemic circulation. The presence of chondrocytes created a vascularization pattern displaying hot spots, which did not form in the cell-free constructs. The difference in vascularization patterns could reflect the upregulation of angiogenic growth factors (e.g., vascular endothelial growth factor) in hypoxic chondrocytes, which stimulated vascularization [64]. Furthermore, IS declined continuously in the cell-free constructs, whereas cell-containing constructs generally displayed a steeper IS throughout the study period.

The diffusion coefficient was significantly higher in the constructs than in native cartilaginous tissue, estimated to be 1.5–2 $\mu\text{m}^2/\text{ms}$ [65], and remained stable, indicating beneficial diffusion properties of the bioink. The constructs showed no tendency to disintegrate over 90 days in vivo, as shown macroscopically, histologically, or on MR images. The

preserved, and high, diffusion coefficient may well reflect an important microstructural characteristic of the biomaterial—that the preserved diffusion facilitates passive transport of nutrients and oxygen, which allows cells in the construct to survive, proliferate, and eventually create the desired type of tissue. Speculatively, a degrading ink with less favorable diffusion properties would offer a less suitable environment for the cells and hence offer less opportunity to make 3D bioprinting successful. Taken together with the successful vascularization, the favorable diffusion qualities further support 3D bioprinted tissue as a tentative source of tissue for reconstructive purposes.

Histologically, both the cell-free and the chondrocyte-containing constructs had large quantities of vascular structures containing erythrocytes, which corroborated the hypothesized vessel growth, as did the immunohistochemical analysis, which showed endothelial cells lining the tube-like structures, mainly in the grid holes (Fig. 5). The chondrocytes proliferated, as judged by their even distribution and clustering and the production of GAG and collagen type II. Interestingly, chondrocytes were found in the biomaterial at the same distances from the grid holes throughout the sections, presumably where the oxygen pressure was most adequate. Visually, this created a halo-like zone around the best perfused areas (i.e., grid holes).

Proximity to blood circulation and optimal conditions for rapid angiogenesis are crucial when creating composite structures, such as the external ear. Unlike cartilaginous tissue, skin and adipose tissues cannot rely on diffusion. In this study, we used chondrocytes to secrete angiogenic factors and grid holes to facilitate the ingrowth of blood vessels. The bioink and cartilaginous tissue were not infiltrated by vessels. We did not find any hypertrophic chondrocytes or other signs of ossification.

We have previously shown long-term data for cartilaginous constructs in vivo [66]. In that study, no indications of hypertrophic transformation or ossification were observed. In native, periarticular cartilage, the transformation zone is characterized by progressive hypertrophy, calcification, and subsequent bone formation. However, in our studies, the chondrocyte phenotype is preserved and histologically displays healthy, proliferating chondrocytes over at least 10 months. One instigating factor for bone transformation in the periarticular zones is compressive, axial forces. Also, specific transformation factors present in, for example, synovial fluid drive the endochondral ossification process in a joint. In our studies, no such external factors affect the subcutaneously implanted constructs. Supposedly, this is one explanation for why no transformation is detected.

Cartilage is an avascular, aneural, and alymphatic tissue with limited ability to regenerate. However, chondrocytes are very robust and resilient, making them suitable for basic research in tissue engineering. Many research groups have developed viable methods to create tissues of various kinds but failed to scale up the dimensions due to a lack of vascularization. Our objective in the present study was to evaluate a clinically viable reconstructive method for bioprinted tissue, focusing especially on the crucial vascularization process. Potentially, further understanding of angiogenesis can bring us closer to tissue engineered constructs with larger dimensions.

This study was limited by the difficulty of ensuring identical conditions between each experimental time point and between individual mice. The main source of error in the diffusion data may be susceptibility-related artifacts due to proximity to extracorporeal air, resulting in image shearing. Furthermore, postoperative artifacts, such as subcutaneous air, may displace pixels in the images, complicating their interpretation early after surgery. Moreover, reproducibility-related effects due to geometrical misalignment between repeated experiments affect the results of DCE perfusion measurements, which are dependent on subjectively drawn regions-of-interest (ROIs). For example, perfusion was higher in the capsule surrounding each implant than in the implant. Including the capsule in the ROI would inadvertently bias the results. An alternative to ROI analysis is to subjectively assess the appearance of the DCE parameter maps over time, but this approach precludes statistical analysis. Also, the amount of contrast

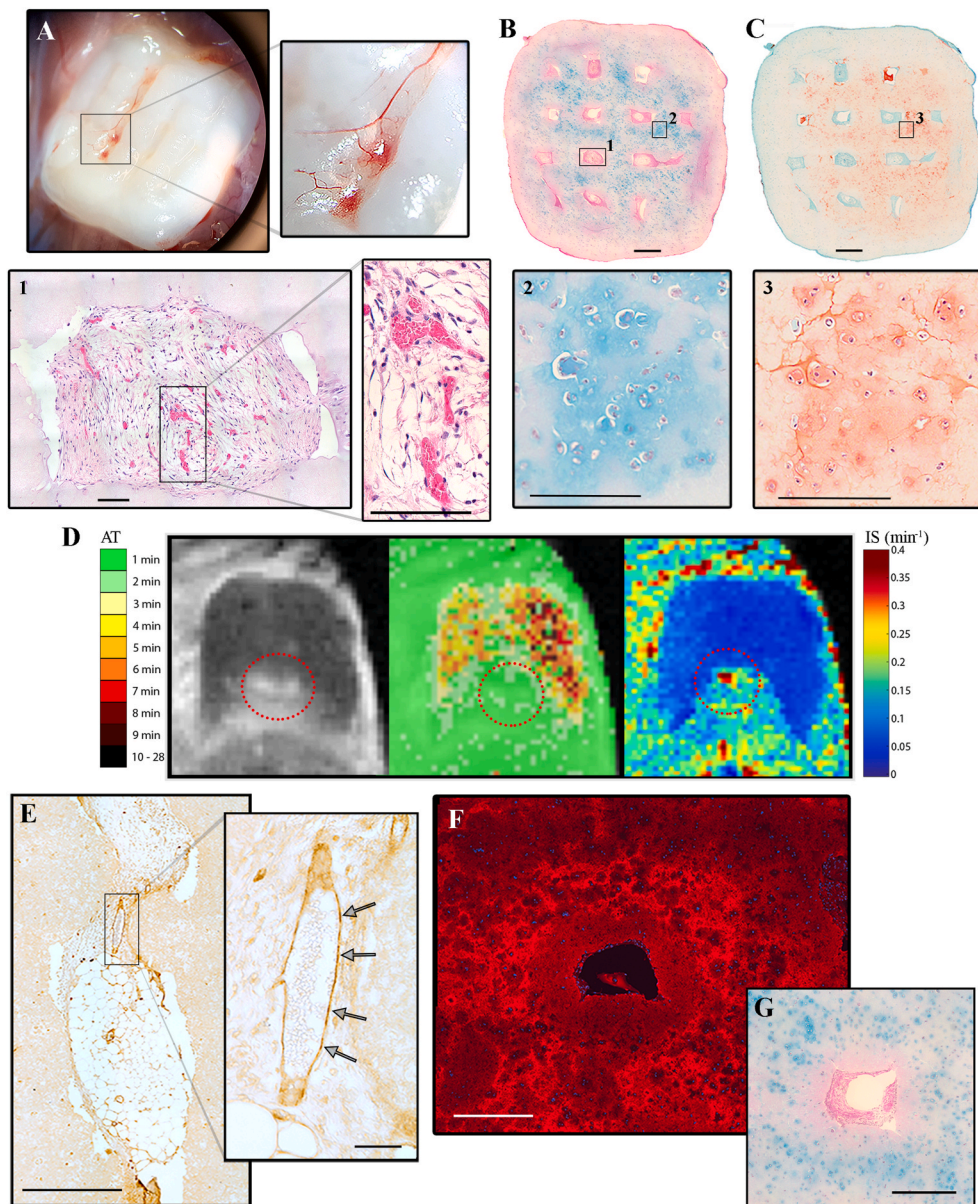


Fig. 5. Cell-containing constructs. (A) Macroscopic appearance of a representative cell-containing construct. A magnified image shows small capsular vessels growing into the grid holes. (B and C) Histological core sections were stained with ABvG and Safranin-O. (2) Magnifications show chondrocytes surrounded by GAGs (cloudy blue) in the extracellular matrix. (3) Safranin-O staining reveals proteoglycans (cloudy orange) in the extracellular matrix surrounding the chondrocytes, corresponding well to the GAG-positive areas. (1) Magnifications of a grid hole containing vessels and erythrocytes; staining with hematoxylin-eosin. (D) Color-coded parametric maps of AT and IS reveal areas of high contrast throughput (i.e., hot spots; encircled in red), corresponding well to the location of the vascularized grid holes. (E) Immunohistochemical analyses with anti-CD31 antibody show dense vascular structures lined with endothelial cells (arrows) inside a grid hole. (F) Immunohistochemical analysis of type 2 collagen show positive areas in the extracellular matrix surrounding the chondrocyte clusters. See Fig. S13 for details in magnification. (G) Outtake from (B) shows the ABvG stained surroundings of one grid hole where the GAG-positive areas are corresponding well to the type 2 collagen-positive areas in (F). (For interpretation of the references to color in this figure legend, the reader is referred to the Web version of this article.)

agent and the injection time in relation to the receiving vessel's volume affects the signal intensity. These uncertainties make it challenging to compare mice within a group or in different groups (carrying different constructs). More studies are needed to further evaluate the MRI analysis of artificial tissues to exploit the full potential of this imaging technique.

Autologous 3D bioprinted cartilaginous tissue has significant clinical potential in reconstructive surgery. Whether the need is for alar cartilage to stabilize a reconstructed nose wing, or even a whole cartilage scaffold for an auricle, delivery of oxygen and nutrients to the cells is crucial. Our study indicates that grid formation in 3D bioprinted constructs containing chondrocytes promotes angiogenesis *in vivo* and that this process can be further understood by using noninvasive MRI methods.

In summary, our findings provide important information on vascularization of 3D bioprinted tissue—a critical step in the translation of bioengineered tissue into clinical practice. The favorable diffusion properties of nanocellulose/alginate bioink and the ingrowth of blood vessels from the host into the gridded structure are fundamentals for increasing the size and biological complexity of 3D bioprinted constructs as a source of clinically relevant tissues for reconstructive purposes.

4. Materials and methods

4.1. Study design

Twenty 8-week-old female BALB/c nude mice (Scanbur) were randomly assigned to two groups, one implanted with chondrocyte-containing constructs ($n = 10$) and one with cell-free constructs ($n = 10$), and studied for 90 days. The number of mice was based upon the maximum number of MRI sessions that were logistically feasible. In the manuscript and supplementary data, all 20 mice are accounted for, and images and data from all constructs are presented. The study was not blinded. The MR images were briefly analyzed during each scanning session, and constructs were selected for further scanning based on technical quality. The ARRIVE Guidelines Checklist [67] was used to report and describe our methods and results.

4.2. Cell source and cell expansion

Human nasoseptal cartilage biopsies were obtained from male donors [age range: 24–40 years; average: 34 ± 5.97 ($n = 6$)] during routine

surgery (i.e., septoplasties or septorhinoplasties) at the Department of Otorhinolaryngology, Head and Neck Surgery, Charité-Medical University (Berlin, Germany). All cartilage samples were first rinsed in sterile 0.1 M phosphate-buffered saline (PBS) and subsequently in standard culture medium [Dulbecco's modified Eagle medium/F-12 (DMEM; 1:1; Life Technologies, Waltham, MA, USA) supplemented with 10% fetal bovine serum (FBS; HyClone; GE Healthcare, South Logan, UT, USA) and 1% penicillin/streptomycin (P/S; Biochrom, Holliston, MA, USA)] under sterile conditions. Adherent non-cartilaginous tissues, including the perichondrium and epithelium, were removed.

To isolate human primary nasal chondrocytes (hNCs), cartilage samples were sliced into 1 mm × 1 mm pieces, and after discarding the medium, transferred to pronase (Serva, Heidelberg, Germany) digestion solution [10 mL; 20 mg/mL (2%) pronase in DMEM supplemented with 1% P/S without FBS]. For the first round of pronase digestion, samples were incubated at 37 °C and 5% CO₂ for 45 min–60 min under continuous agitation, after which the pronase solution was discarded, and pre-digested cartilage samples were washed twice with sterile 1 × PBS. For the final digestion, cartilage samples were transferred to collagenase (Gibco; Life Technologies, Carlsbad, CA, USA) digestion solution [1 mg/mL (0.1%) collagenase in DMEM complemented with 0.5% FBS and 1% P/S] and incubated for 16 h–18 h at 37 °C and 5% CO₂ with continuous shaking. After centrifugation, total cell number and viability were determined using the Trypan blue exclusion method (Table S2). Subsequently, hNCs were seeded for amplification at an initial density of 5×10^3 cells/cm² and cultured in a standard culture medium. Upon reaching 80%–90% confluence, cells were detached, counted (Cell Counter; Thermo Fisher Scientific, Waltham, MA, USA), and cryopreserved to ensure equal treatment of all hNCs harvested from different patients. Cryopreserved hNCs were thawed and expanded once in monolayer culture to obtain a sufficient number of cells. Upon reaching 80%–90% confluence, cells were detached, counted, and resuspended in a standard culture medium. All experiments were conducted using hNCs at passage two.

4.3. Preparation of bioinks and 3D bioprinting

The hNCs were gently mixed with bioink consisting of an 80:20 mixture of tunicate nanocellulose (Ocean TuniCell, AS, Blomsterdalen, Norway) and alginate (SLG100; NovaMatrix, Sandvika, Norway). The hNC to ink ratio was 1:10, and the initial cell density was 10×10^6 cells/mL of bioink. Cell-free samples were also prepared. The bioink was 3D bioprinted (Inkredible+, CELLINK) as gridded square constructs (10 × 10 × 3 mm) with a 25% rectilinear infill. An 18G conical nozzle was used, and the printing pressure was 11–13 kPa. The constructs were crosslinked with 0.5 mM CaCl₂ for 5 min, washed in culture medium (Dulbecco's modified Eagle medium/F-12 (DMEM; 1:1; Life Technologies, Waltham, MA, USA), and implanted within 1 h after printing.

4.4. Animal model

The mice were anesthetized with isoflurane (Isoflurane Baxter, Baxter International), and the 3D-bioprinted constructs were implanted subcutaneously in the neck/back region. No antibiotics were used. Each mouse was identified with an earmark.

4.5. MRI

During MRI experiments, anesthesia was maintained with 2–3% isoflurane (Isoba vet., Schering-Plough Animal HealthK). Body temperature was maintained with a heating pad on the animal holder, and respiration was monitored with a pressure-sensitive pad (SA Instruments). Gadolinium-based contrast agent solution (0.1 M Gd-DTPA, Dotarem, Gothia Medical; 0.3 mmol/kg body weight) was administered with a peripheral venous catheter placed in a tail vein and connected to a 1-mL syringe by an infusion line extending out of the magnet bore.

MRI was done with a preclinical, horizontal bore 7 T MR system (Bruker BioSpin 70/20AS AVANCE 1 using ParaVision 5.1) equipped with a maximum 400 mT/m gradient system and a 30-mm transmit/receive volume coil (RAPID Biomedical). Global first- and second-order shimming was used to improve field homogeneity. Conventional two-dimensional (2D) T2-weighted images of the implant and surrounding anatomy were acquired in axial and coronal views with the rapid acquisition with relaxation enhancement (RARE) sequence: repetition time (TR) 3000 ms, echo time (TE) = 24 ms, turbo factor = 4, number of signal averages (NSA) = $6150^2 \mu\text{m}^2$ in-plane resolution, and slice thickness of 500 μm (axial) or 400 μm (coronal). DCE images were acquired with the 2D, retrospectively gated, intra-gate, fast low-angle shot sequence: TR = 13 ms, TE = 1.1 ms, NSA = 11,500 repetitions over ~32 min for the reconstruction of 32 time frames, $300^2 \mu\text{m}^2$ in-plane resolution, and 1000- μm slice thickness. The navigator signal was derived from a 45-mm-thick saturation slice including the image slices in parallel orientation. At the start of the acquisition of the sixth frame (5 min after the scan was started), the contrast agent was injected over 10 s. DWI was done with a 2D single-shot, spin-echo echo-planar imaging sequence: TR = 3500 ms, TE = 25 ms, NSA = 14, 5 acquisitions without diffusion gradients ($b = 0 \text{ s/mm}^2$) and 12 acquisitions at b -values of 50, 200, 400, and 900 s/mm^2 , in 3 orthogonal diffusion directions. Gradient duration was 4 ms and separation was 9 ms. EPI image readout: $250^2 \mu\text{m}^2$ in-plane resolution, 700- μm slice thickness.

Each MRI session took about 75 min per mouse, after which the mice were returned to their cages and monitored until fully alert. After the fourth and last scanning, the mice were euthanized by cervical dislocation while still under anesthesia. The MRI data were post-processed with MATLAB (R2019b, The MathWorks) with standard and in-house developed functions and scripts.

DCE MR signal intensity enhancement in the implant after contrast injection was analyzed voxel-wise as follows. The baseline voxel intensity was calculated as the mean signal intensity of the first five frames. The AT was defined as the time required from injection to the point at which signal intensity in a voxel was twice the voxel noise level above the baseline value. Voxel noise was defined as the standard deviation of the voxel signal values of the five frames before contrast injection. Functional maps were constructed by superimposing color-coded AT values on the baseline image (Fig. S5). The detected MRI signal intensity is relative to baseline, which potentially differs from session to session. Each baseline was therefore calibrated by comparing the signal intensity of the construct with that of native muscle tissue. The DCE signal intensity was also quantified by using region-of-interest (ROI) maps from the MRI data, creating graphs that enabled further interpretations and comparisons between the different constructs.

Diffusion coefficient maps were calculated for each voxel by segmented bi-exponential model fitting, which renders the diffusion coefficient minimally affected by perfusion effects by fitting it only to b -values of 200, 400, and 900 s/mm^2 [40]. The median diffusion coefficient of each implant was calculated from all voxels within the implant by manually delineating it on the $b = 0 \text{ s/mm}^2$ (B0) images. Slices covering the edges of the implant were excluded to avoid partial volume effects.

4.6. Morphology

For *in vitro* controls on day 0, the printed constructs were directly fixed in calcium-saturated (4%) paraformaldehyde and stored at 4 °C. All constructs were paraffinized, sectioned (5 μm thick) horizontally, and mounted on glass slides (Fig. S1). On day 90, the constructs were retrieved, macroscopically examined, marked for orientation with tissue dye (Thermo Fisher Scientific), fixed in calcium-saturated 4% paraformaldehyde, and stored at 4 °C until paraffinization and sectioning. Deparaffinized sections were stained with hematoxylin-eosin, ABVG, and Safranin-O. The sections were scanned with a Nikon Eclipse 90i epifluorescence microscope equipped with a Nikon DS-Fi2 color head

camera and a NIS-Elements imaging software suite (vD4.10.02; Nikon Instruments). The images were imported into PhotoShop 2020 (Adobe Systems) and cropped, white-balanced, and linearly adjusted for contrast and exposure.

4.7. Immunohistochemistry

Endothelial cells were detected with a human anti-CD31 antibody (clone EP3095, product no. ab134168, Abcam; 1:200). Human liver tissue served as a positive control. A rabbit IgG isotype control (clone EPR25A, product no. ab172730, Abcam) and secondary antibodies alone served as negative controls to differentiate background signal from specific antibody staining. CD31-positive cells were identified with the Vectastain Elite ABC kit, a biotinylated secondary antibody (PK6101; BioNordika), and ImmPACT DAB (H-4000; BioNordika).

To assess collagen production in the extracellular matrix, the sections were incubated first with a monoclonal mouse antihuman type 2 collagen antibody IgG (Clone II-4C11, catalog no. 63171, MP Bio-medicals; 1:300) and then with goat anti-mouse IgG conjugated with AlexaFluor 546 (A11030, Invitrogen; 1:300), and the mounting solution was applied (ProLong Gold antifade mountant with DAPI; Invitrogen). Cartilage pellets from horse served as a positive control. A monoclonal mouse IgG antibody (mouse IgG1 K isotype control purified, catalog no. 14-4714-82, eBioscience, Thermo Fisher Scientific; 1:75) served as control.

Ethical approval

Cartilage harvesting was approved by the Ethics Committee at Charité Universitätsmedizin in Berlin (No.: EA1/169_12), and all patients gave informed consent. The study was approved by the Ethics Committee for animal experiments at Sahlgrenska University Hospital (Dnr 119–2015 and 36–2016). Ethical approval for the positive controls in the immunohistological analyses was issued by the Ethics Committee at the University of Gothenburg (Gothenburg, Sweden, Dnr S040-01). All animal experiments were done following institutional, national, and European guidelines and regulations at the core facility for experimental biomedicine at the University of Gothenburg.

4.8. Statistics

Histograms of the diffusion coefficients showed normal distribution, so a normality test was unnecessary. The medians and interquartile ranges were calculated and graphed with SPSS (v22.0; IBM SPSS) and Microsoft Excel (v16.28).

Funding

This work was supported by Sahlgrenska University Hospital and Sahlgrenska Academy at the University of Gothenburg. This study was financed by grants from the Swedish state under the ALF agreement between the Swedish government and the county councils (ALFGBG-716621). The Knut and Alice Wallenberg Foundation provided financial support in the framework of the Wallenberg Wood Science Center. Furthermore, this study was supported by grants from the Gothenburg Medical Society, the Wilhelm and Martina Lundgren Foundation for Science, the Mary von Sydow Foundation, the Magnus Bergvalls Foundation, the Sigurd and Elsa Goljes Foundation, and the Ann-Mari and Per Ahlqvist Foundation.

Data and materials availability

All data from this study are shown in the paper and the supplementary section.

Declaration of competing interest

The authors declare that they have no known competing financial interests or personal relationships that could have appeared to influence the work reported in this paper.

Acknowledgments

We thank the staff at Experimental Biomedicine at Gothenburg University for their support with the animal experiments. We also thank the laboratory staff at the Department of Clinical Chemistry and Transfusion Medicine at the Sahlgrenska Academy (especially Mona Engström and Camilla Brantsing) for support with the immunohistochemical analyses. Furthermore, the cartilage samples have been kindly provided by Dr. Katharina Stölzel at the Department of Otorhinolaryngology, Head and Neck Surgery at Charité Universitätsmedizin, Campus Charité Mitte in Berlin, Germany. We would also like to acknowledge Dr. Silke Schwarz and Prof. Dr. Gundula Schulze-Tanzil at the Department of Anatomy at Paracelsus Medical University in Nürnberg, Germany, who performed the cell isolation and cultivation procedures. The authors would also like to thank Stephen Ordway for editing the manuscript.

Appendix A. Supplementary data

Supplementary data to this article can be found online at <https://doi.org/10.1016/j.biomaterials.2021.121002>.

Credit author statement

P.A., M.A., K.S., P.G., and L.K. designed the study and did *in vivo* experiments. L.S.O did *in vitro* experiments and all the 3D bioprinting procedures. M.M. optimized the MRI experiments and developed the MatLab scripts for postprocessing. M.M., P.A., M.A., K.S., and L.K. analyzed and interpreted the MRI data. A.L. provided laboratory expertise and did the immunohistochemical analysis. P.A., M.A., K.S., and L.K. wrote the paper.

References

- [1] A. Lindahl, From gristle to chondrocyte transplantation: treatment of cartilage injuries, *Philos. Trans. R. Soc. Lond. B Biol. Sci.* 370 (2015) 20140369.
- [2] H.W. Kang, J.J. Yoo, A. Atala, Bioprinted scaffolds for cartilage tissue engineering, *Methods Mol. Biol.* 1340 (2015) 161–169.
- [3] R. Langer, J. Vacanti, Advances in tissue engineering, *J. Pediatr. Surg.* 51 (2016) 8–12.
- [4] F. Firmin, A. Marchac, A novel algorithm for autologous ear reconstruction, *Semin. Plast. Surg.* 25 (2011) 257–264.
- [5] G. Osorno, Autogenous rib cartilage reconstruction of congenital ear defects: report of 110 cases with Brent's technique, *Plast. Reconstr. Surg.* 104, 1951–1962; discussion 1963–1954 (1999).
- [6] P. Carmeliet, R.K. Jain, Angiogenesis in cancer and other diseases, *Nature* 407 (2000) 249–257.
- [7] H.W. Kang, S.J. Lee, I.K. Ko, C. Kengla, J.J. Yoo, A. Atala, A 3D bioprinting system to produce human-scale tissue constructs with structural integrity, *Nat. Biotechnol.* 34 (2016) 312–319.
- [8] M. Radisic, J. Malda, E. Epping, W. Geng, R. Langer, G. Vunjak-Novakovic, Oxygen gradients correlate with cell density and cell viability in engineered cardiac tissue, *Biotechnol. Bioeng.* 93 (2006) 332–343.
- [9] D. Richards, J. Jia, M. Yost, R. Markwald, Y. Mei, 3D Bioprinting for vascularized tissue fabrication, *Ann. Biomed. Eng.* 45 (2017) 132–147.
- [10] J. Rouwkema, N.C. Rivron, C.A. van Blitterswijk, Vascularization in tissue engineering, *Trends Biotechnol.* 26 (2008) 434–441.
- [11] R.L. Carrier, M. Rupnick, R. Langer, F.J. Schoen, L.E. Freed, G. Vunjak-Novakovic, Perfusion improves tissue architecture of engineered cardiac muscle, *Tissue Eng.* 8 (2002) 175–188.
- [12] J.O. Den Buijs, L. Lu, S.M. Jorgensen, D. Dragomir-Daescu, M.J. Yaszemski, E. L. Ritman, Solute transport in cyclically deformed porous tissue scaffolds with controlled pore cross-sectional geometries, *Tissue Eng.* 15 (2009) 1989–1999.
- [13] S.J. Hollister, Porous scaffold design for tissue engineering, *Nat. Mater.* 4 (2005) 518–524.
- [14] J. Hu, X. Sun, H. Ma, C. Xie, Y.E. Chen, P.X. Ma, Porous nanofibrous PLLA scaffolds for vascular tissue engineering, *Biomaterials* 31 (2010) 7971–7977.

- [15] V.S. Joshi, N.Y. Lei, C.M. Walthers, B. Wu, J.C. Dunn, Macroporosity enhances vascularization of electrospun scaffolds, *J. Surg. Res.* 183 (2013) 18–26.
- [16] R. Maidhof, N. Tandon, E.J. Lee, J. Luo, Y. Duan, K. Yeager, E. Konofagou, G. Vunjak-Novakovic, Biomimetic perfusion and electrical stimulation applied in concert improved the assembly of engineered cardiac tissue, *J. Tissue Eng Regen Med* 6 (2012) e12–23.
- [17] M.M. Nava, L. Draghi, C. Giordano, R. Pietrabissa, The effect of scaffold pore size in cartilage tissue engineering, *J. Appl. Biomater. Funct. Mater.* 14 (2016) e223–229.
- [18] F.J. O'Brien, B.A. Harley, M.A. Waller, I.V. Yannas, L.J. Gibson, P.J. Prendergast, The effect of pore size on permeability and cell attachment in collagen scaffolds for tissue engineering, *Technol. Health Care* 15 (2007) 3–17.
- [19] L.E. Bertassoni, M. Cecconi, V. Manoharan, M. Nikkiah, J. Hjortnaes, A.L. Cristino, G. Barabaschi, D. Demarchi, M.R. Dokmeci, Y. Yang, A. Khademhosseini, Hydrogel bioprinted microchannel networks for vascularization of tissue engineering constructs, *Lab Chip* 14 (2014) 2202–2211.
- [20] M. Burghartz, T. Gehrke, K. Störck, R. Staudenmaier, V. Mandlik, C. Schurr, N. Hoang, R. Hagen, N. Kleinsasser, Vascularization of engineered cartilage constructs in a mouse model, *Cell Tissue Res.* 359 (2015) 479–487.
- [21] G. Gao, A.F. Schilling, K. Hubbell, T. Yonezawa, D. Truong, Y. Hong, G. Dai, X. Cui, Improved properties of bone and cartilage tissue from 3D inkjet-bioprinted human mesenchymal stem cells by simultaneous deposition and photocrosslinking in PEG-GelMA, *Biotechnol. Lett.* 37 (2015) 2349–2355.
- [22] K. Nakano, K. Murata, S. Omokawa, M. Akahane, T. Shimizu, K. Kawamura, K. Kawate, Y. Tanaka, Promotion of osteogenesis and angiogenesis in vascularized tissue-engineered bone using osteogenic matrix cell sheets, *PLA. Reconstr. Surg.* 137 (2016) 1476–1484.
- [23] D.H. Nguyen, S.C. Stapleton, M.T. Yang, S.S. Cha, C.K. Choi, P.A. Galie, C.S. Chen, Biomimetic model to reconstitute angiogenic sprouting morphogenesis in vitro, *Proc. Natl. Acad. Sci. U. S. A.* 110 (2013) 6712–6717.
- [24] R. Sooppan, S.J. Paulsen, J. Han, A.H. Ta, P. Dinh, A.C. Gaffey, C. Venkataraman, A. Trubelja, G. Hung, J.S. Miller, P. Atluri, In vivo anastomosis and perfusion of a three-dimensionally-printed construct containing microchannel networks, *Tissue Eng. C Methods* 22 (2016) 1–7.
- [25] W. Risau, I. Flamme, *Vasculogenesis. Annu Rev Cell Dev Biol* 11 (1995) 73–91.
- [26] P.A. Fleming, W.S. Argraves, C. Gentile, A. Neagu, G. Forgacs, C.J. Drake, Fusion of uniluminal vascular spheroids: a model for assembly of blood vessels, *Dev. Dynam.* 239 (2010) 398–406.
- [27] C. Gentile, P.A. Fleming, V. Mironov, K.M. Argraves, W.S. Argraves, C.J. Drake, VEGF-mediated fusion in the generation of uniluminal vascular spheroids, *Dev. Dynam.* 237 (2008) 2918–2925.
- [28] K. Jakab, A. Neagu, V. Mironov, G. Forgacs, Organ printing: fiction or science, *Biorheology* 41 (2004) 371–375.
- [29] K. Jakab, C. Norotte, F. Marga, K. Murphy, G. Vunjak-Novakovic, G. Forgacs, Tissue engineering by self-assembly and bio-printing of living cells, *Biofabrication* 2 (2010), 022001.
- [30] V. Lee, G. Singh, J.P. Trasatti, C. Björnsson, X. Xu, T.N. Tran, S.S. Yoo, G. Dai, P. Karande, Design and fabrication of human skin by three-dimensional bioprinting, *Tissue Eng. C Methods* 20 (2014) 473–484.
- [31] J. Rouwkema, A. Khademhosseini, Vascularization and angiogenesis in tissue engineering: beyond creating static networks, *Trends Biotechnol.* 34 (2016) 733–745.
- [32] R.P. Visconti, V. Kasyanov, C. Gentile, J. Zhang, R.R. Markwald, V. Mironov, Towards organ printing: engineering an intra-organ branched vascular tree, *Exp. Opin. Biol. Ther.* 10 (2010) 409–420.
- [33] P. Carmeliet, Mechanisms of angiogenesis and arteriogenesis, *Nat. Med.* 6 (2000) 389–395.
- [34] S. Ahlawat, L.M. Fayad, Diffusion weighted imaging demystified: the technique and potential clinical applications for soft tissue imaging, *Skeletal Radiol.* 47 (2018) 313–328.
- [35] S.H. Lee, J.H. Lee, K.H. Cho, Effects of human adipose-derived stem cells on cutaneous wound healing in nude mice, *Ann. Dermatol.* 23 (2011) 150–155.
- [36] G. Petralia, P.E. Summers, A. Agostini, R. Ambrosini, R. Cianci, G. Cristel, L. Calistri, S. Colagrande, Dynamic contrast-enhanced MRI in oncology: how we do it, *Radiol. Med.* (2020).
- [37] J.G. Raya, Techniques and applications of in vivo diffusion imaging of articular cartilage, *J. Magn. Reson. Imag.* 41 (2015) 1487–1504.
- [38] H.C. Thoeny, F. De Keyser, Extracranial applications of diffusion-weighted magnetic resonance imaging, *Eur. Radiol.* 17 (2007) 1385–1393.
- [39] S.P. Li, A.R. Padhani, Tumor response assessments with diffusion and perfusion MRI, *J. Magn. Reson. Imag.* 35 (2012) 745–763.
- [40] O. Jalnefjord, M. Andersson, M. Montelius, G. Starck, A.K. Elf, V. Johanson, J. Svensson, M. Ljungberg, Comparison of methods for estimation of the intravoxel incoherent motion (IVIM) diffusion coefficient (D) and perfusion fraction (f), *Magma* 31 (2018) 715–723.
- [41] J.H.e. a. Chung, Bio-ink properties and printability for extrusion printing living cells, *Biomater. Sci-UK* 1 (2013) 763–773.
- [42] K. Holzl, S. Lin, L. Tytgat, S. Van Vlierberghe, L. Gu, A. Ovsianikov, Bioink properties before, during and after 3D bioprinting, *Biofabrication* 8 (2016), 032002.
- [43] I.T. Ozbolat, W. Peng, V. Ozbolat, Application areas of 3D bioprinting, *Drug Discov Today*, 2016.
- [44] J.A. Barron, P. Wu, H.D. Ladouceur, B.R. Ringeisen, Biological laser printing: a novel technique for creating heterogeneous 3-dimensional cell patterns, *Biomed. Microdevices* 6 (2004) 139–147.
- [45] F. Guillemot, A. Souquet, S. Catros, B. Guillotin, Laser-assisted cell printing: principle, physical parameters versus cell fate and perspectives in tissue engineering, *Nanomedicine* 5 (2010) 507–515.
- [46] B. Guillotin, A. Souquet, S. Catros, M. Duocastella, B. Pippenger, S. Bellance, R. Bareille, M. Remy, L. Bordenave, J. Amedee, F. Guillemot, Laser assisted bioprinting of engineered tissue with high cell density and microscale organization, *Biomaterials* 31 (2010) 7250–7256.
- [47] T. Boland, T. Xu, B. Damon, X. Cui, Application of inkjet printing to tissue engineering, *Biotechnol. J.* 1 (2006) 910–917.
- [48] T. Xu, K.W. Binder, M.Z. Albanna, D. Dice, W. Zhao, J.J. Yoo, A. Atala, Hybrid printing of mechanically and biologically improved constructs for cartilage tissue engineering applications, *Biofabrication* 5 (2013), 015001.
- [49] K. Markstedt, A. Mantas, I. Tournier, H. Martinez Avila, D. Hagg, P. Gatenholm, 3D bioprinting human chondrocytes with nanocellulose-alginate bioink for cartilage tissue engineering applications, *Biomacromolecules* 16 (2015) 1489–1496.
- [50] H. Martinez Avila, S. Schwartz, N. Rotter, P. Gatenholm, 3D bioprinting of human chondrocyte-laden nanocellulose hydrogels for patient-specific auricular cartilage regeneration, *Bioprinting* 1–2 (2016) 22–35.
- [51] L. Figueiredo, R. Pace, C. D'Arros, G. Rethore, J. Guicheux, C. Le Visage, P. Weiss, Assessing glucose and oxygen diffusion in hydrogels for the rational design of 3D stem cell scaffolds in regenerative medicine, *J. Tissue Eng Regen Med* 12 (2018) 1238–1246.
- [52] B. Balakrishnan, R. Banerjee, Biopolymer-based hydrogels for cartilage tissue engineering, *Chem. Rev.* 111 (2011) 4453–4474.
- [53] D. Nguyen, D.A. Hagg, A. Forsman, J. Ekholm, P. Nimkingratana, C. Brantsing, T. Kalogeropoulos, S. Zaunz, S. Concaro, M. Brittberg, A. Lindahl, P. Gatenholm, A. Enejder, S. Simonsson, Cartilage tissue engineering by the 3D bioprinting of iPSC cells in a nanocellulose/alginate bioink, *Sci. Rep.* 7 (2017) 658.
- [54] P. Apelgren, M. Amoroso, A. Lindahl, C. Brantsing, N. Rotter, P. Gatenholm, L. Kolby, Chondrocytes and stem cells in 3D-bioprinted structures create human cartilage in vivo, *PLoS One* 12 (2017), e0189428.
- [55] P. Apelgren, M. Amoroso, K. Saljo, A. Lindahl, C. Brantsing, L. Stridh Orrhult, P. Gatenholm, L. Kolby, Skin grafting on 3D bioprinted cartilage constructs in vivo, *PLast Reconstr Surg Glob Open* 6 (2018), e1930.
- [56] J. Stojkowska, B. Bugarski, B. Obradovic, Evaluation of alginate hydrogels under in vivo-like bioreactor conditions for cartilage tissue engineering, *J. Mater. Sci. Mater. Med.* 21 (2010) 2869–2879.
- [57] C.B. Highley, G.D. Prestwich, J.A. Burdick, Recent advances in hyaluronic acid hydrogels for biomedical applications, *Curr. Opin. Biotechnol.* 40 (2016) 35–40.
- [58] C.Y. Ko, K.L. Ku, S.R. Yang, T.Y. Lin, S. Peng, Y.S. Peng, M.H. Cheng, I.M. Chu, In vitro and in vivo co-culture of chondrocytes and bone marrow stem cells in photocrosslinked PCL-PEG-PCL hydrogels enhances cartilage formation, *J. Tissue Eng Regen Med* 10 (2016) E485–E496.
- [59] I.A. Sacui, R.C. Nieuwendael, D.J. Burnett, S.J. Stranick, M. Jorfi, C. Weder, E. J. Foster, R.T. Olsson, J.W. Gilman, Comparison of the properties of cellulose nanocrystals and cellulose nanofibrils isolated from bacteria, tunicate, and wood processed using acid, enzymatic, mechanical, and oxidative methods, *ACS Appl. Mater. Interfaces* 6 (2014) 6127–6138.
- [60] Y. Zhao, C. Moser, M.E. Lindstrom, G. Henriksson, J. Li, Cellulose nanofibers from softwood, hardwood, and tunicate: preparation-structure-film performance interrelation, *ACS Appl. Mater. Interfaces* 9 (2017) 13508–13519.
- [61] Y. Zhao, Y. Zhang, M.E. Lindstrom, J. Li, Tunicate cellulose nanocrystals: preparation, neat films and nanocomposite films with glucosaminans, *Carbohydr. Polym.* 117 (2015) 286–296.
- [62] Y. Zhou, The application of ultrasound in 3D bio-printing, *Molecules* 21 (2016).
- [63] B.P. Venkatesulu, L.S. Mahadevan, M.L. Aliru, X. Yang, M.H. Bodd, P.K. Singh, S. W. Yusuf, J.I. Abe, S. Krishnan, Radiation-induced endothelial vascular injury: a review of possible mechanisms, *JACC Basic Transl Sci* 3 (2018) 563–572.
- [64] C. Maes, I. Stockmans, K. Moermans, R. Van Looveren, N. Smets, P. Carmeliet, R. Bouillon, G. Carmeliet, Soluble VEGF isoforms are essential for establishing epiphyseal vascularization and regulating chondrocyte development and survival, *J. Clin. Invest.* 113 (2004) 188–199.
- [65] A.M. Gillis, M. Gray, D. Burstein, Paper Presented at the 46th Annual Meeting, Orthopaedic Research Society, Orlando, Florida, 2000. March 12–15.
- [66] P. Apelgren, M. Amoroso, K. Saljo, A. Lindahl, C. Brantsing, L. Stridh Orrhult, K. Markstedt, P. Gatenholm, L. Kolby, Long-term in vivo integrity and safety of 3D-bioprinted cartilaginous constructs, *J. Biomed. Mater. Res. B Appl. Biomater.* 109 (2021) 126–136.
- [67] C. Kilkenny, W.J. Browne, I.C. Cuthill, M. Emerson, D.G. Altman, Improving bioscience research reporting: the ARRIVE guidelines for reporting animal research, *Osteoarthritis Cartilage* 20 (2012) 256–260.